

Investigating Electronic, Optical, and Phononic Properties of Bulk γ - M_2ON_2 and β - $M_7O_8N_4$ (M = Hf and Zr) Insulators Using Density Functional Theory

Author:

Thapa, B; Patterson, RJ; Conibeer, G; Shrestha, S

Publication details:

ACS Omega

v. 7

Chapter No. 11

Medium: Electronic-eCollection

pp. 9196 - 9205

2470-1343 (ISSN)

Publication Date:

2022-03-22

Publisher DOI:

<https://doi.org/10.1021/acsomega.1c05649>

Downloaded from http://hdl.handle.net/1959.4/unsworks_80928 in <https://unsworks.unsw.edu.au> on 2024-05-18

Investigating Electronic, Optical, and Phononic Properties of Bulk γ - M_2O_N and β - $M_7O_8N_4$ ($M = \text{Hf}$ and Zr) Insulators Using Density Functional Theory

Bharat Thapa,* Robert John Patterson, Gavin Conibeer, and Santosh Shrestha



Cite This: *ACS Omega* 2022, 7, 9196–9205



Read Online

ACCESS |



Metrics & More

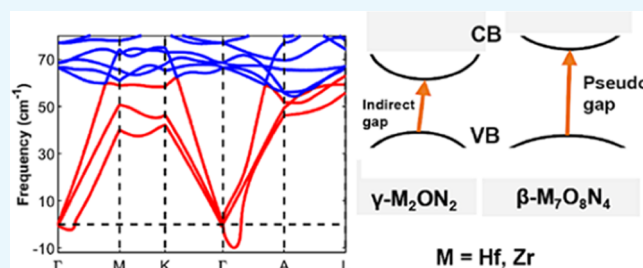


Article Recommendations



Supporting Information

ABSTRACT: Hafnium and zirconium oxynitrides have similar properties, yet a consolidated investigation of their intrinsic properties has not been carried out. In this paper, we perform first-principles density functional theory calculations of γ - and β -phase hafnium and zirconium oxynitrides, which show that the γ - M_2O_N ($M = \text{Hf}$ and Zr) is an indirect band-gap (E_g) insulator, while the β - $M_7O_8N_4$ has a “pseudo-direct” type of E_g . β -phase has higher E_g than γ -phase, with concomitant disappearance of the conduction band tail. Optical properties in γ - M_2O_N show that the anisotropy is negligible, and the optical constant values are in the range of other superhard materials. Phonon calculations present peculiar characteristics such as a small phonon band gap in γ - Hf_2O_N and imaginary phonon frequencies in β -phases relating to lattice instability. The phononic properties are unfavorable for their potential use as an absorber material of the hot carrier solar cell—an emerging photovoltaic concept.



1. INTRODUCTION

Hafnium and zirconium oxynitrides are an interesting class of materials having applications in diverse areas such as renewable energy generation, semiconductor devices, corrosion-resistance coating, and temperature sensors, as discussed below. They are characterized by excellent hardness and exhibit polymorphism such that the proportion of O and N in the material can vary depending upon the growth conditions. Since O is more electronegative than N while N is more polarizable than O, the optical properties and electronic band-gap (E_g) values can be tuned.^{1–4}

Hafnium oxynitrides in the form of RHfO_2N perovskites ($R =$ rare earth metals such as La, Nd, and Sm)⁵ and ZrO_xN_y ^{6,7} are promising photocatalytic materials for water splitting as they have a higher E_g than the minimum threshold (1.23 eV) and good photocorrosion resistance. Photocatalytic water splitting is a clean energy harvesting technique in which H_2 from water is extracted, exploiting suitable E_g and appropriate band offset values (with respect to water's reduction and oxidation potentials) of semiconductors driven by photo-illumination.⁸ Ultrathin HfO_xN_y thin film is an active research material for high- k dielectric material in metal–insulator–semiconductor (MIS) devices, owing to high dielectric constant, low equivalent oxide thickness (EOT), and low leakage current.⁹ Further, HfO_xN_y is also a promising “solid electrolyte” in electrochemical metallization memory,¹⁰ a type of resistive random access memory (RRAM) devices based on the metal–insulator–metal (MIM) architecture.¹¹ The application of both of these oxynitrides extends to temperature

sensing devices due to excellent temperature sensitivity and thermal stability.¹² Recently, a preliminary assessment indicated that HfO_xN_y can have potential application in a hot carrier solar cell (HCSC).¹³ A HCSC is a so-called third-generation photovoltaic (PV) concept, which can, in principle, generate PV power with an efficiency of up to 66% in 1 sun.¹⁴ Despite multiple potential applications, there has been a limited theoretical study on these materials that explores electronic properties and no study regarding the optical and phononic properties to the best of our knowledge. In this paper, electronic, optical, and phononic properties of γ - M_2O_N and β - $M_7O_8N_4$ ($M = \text{Hf}$ or Zr) phases are studied using the density functional theory (DFT) method and the results are consolidated in these isostructural compounds for the first time.

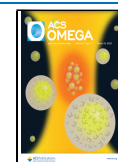
2. CRYSTAL STRUCTURE

Zirconium oxynitrides exist in many different phases such as γ - Zr_2O_N , β - $\text{Zr}_7\text{O}_8\text{N}_4$, and β' - $\text{Zr}_7\text{O}_{11}\text{N}_2$ with increasing O quantities in these polymorphs, respectively.^{15–17} The Hf counterparts are isostructural, owing to the very similar atomic

Received: October 9, 2021

Accepted: January 18, 2022

Published: March 7, 2022



radii of Hf^{4+} and Zr^{4+} and their position in the same group (IVB) of the periodic table.^{2,18} X-ray and neutron diffraction techniques suggested that the crystal structure of $\gamma\text{-Zr}_2\text{ON}_2$ is cubic bixbyite type.¹⁷ Examples of the bixbyite-type structures are $c\text{-V}_2\text{O}_3$,¹⁹ $c\text{-Ce}_2\text{O}_3$, and $c\text{-La}_2\text{O}_3$, which are body-centered cubic with space group $Ia\bar{3}$ [206]. Because the difference is so subtle, it is not trivial to distinguish if Zr_2ON_2 crystallizes in $Ia\bar{3}$ [206] or $Ibca$ [73] (a body-centered orthorhombic structure). Nevertheless, it was concluded that the N and O anions in the crystal are statistically disordered,^{17,20} and the structure is normally modeled with space group $Ibca$. The structure of $\beta\text{-Zr}_7\text{O}_8\text{N}_4$ was determined to be $R\bar{3}$ from powder XRD techniques and is described as rhombohedrally distorted fluorite type.¹⁶ The $\beta\text{-Zr}_7\text{O}_{11}\text{N}_2$ is similar to $\beta\text{-Zr}_7\text{O}_8\text{N}_4$ (sometimes commonly called the “ β ” family) and belongs to the same space group $R\bar{3}$ but has lattice parameter c almost double that of the latter.¹⁶ In this work, $\beta\text{-M}_7\text{O}_{11}\text{N}_2$ is not investigated because of the uncertainty in the positions of N and O atoms in the unit cell.²¹ Based on X-ray diffraction, the β -family are referred to as “pseudo-cubic” due to their resemblance with cubic HfO_2 .²

The crystal structures of $\gamma\text{-M}_2\text{ON}_2$ and $\beta\text{-M}_7\text{O}_8\text{N}_4$ and the local environments are shown in Figure 1. In $\gamma\text{-M}_2\text{ON}_2$, the M^{4+} cation is coordinated by 4 N and 2 O anions forming a highly distorted octahedron. The building blocks of the $\beta\text{-M}_7\text{O}_8\text{N}_4$ are the so-called “Bevan clusters”, designated as A_7X_{12} and are obtained from a slight modification of the Zr_7O_{14} unit—a building block of the cubic zirconia.^{16,22} In this environment, the central metal cation is 6-fold-coordinated by

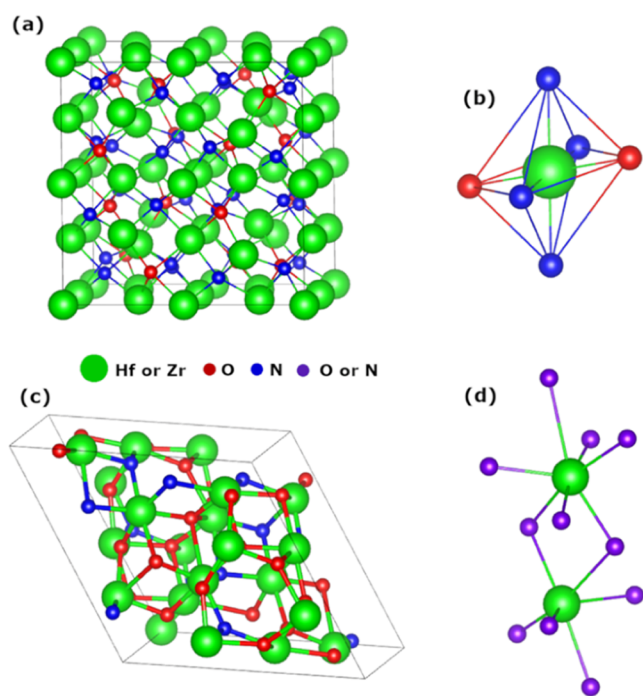


Figure 1. Crystal structure of the oxynitrides. (a) Conventional unit cell of $\gamma\text{-M}_2\text{ON}_2$, belonging to $Ibca$ [73]. (b) Local environment around the M^{4+} cation of $\gamma\text{-M}_2\text{ON}_2$. (c) Conventional unit cell of $\beta\text{-M}_7\text{O}_8\text{N}_4$, belonging to $R\bar{3}$ [148]. (d) Local environment around the M^{4+} cation in $\beta\text{-M}_7\text{O}_8\text{N}_4$. M at the center of the Bevan cluster (bottom green sphere) is 6-fold-coordinated by the anions, while the remaining cations (e.g., the top green sphere) are 7-fold-coordinated by the anions. Since the anions are statistically distributed, the positions of O and N anions are not specific.

the anions, while the remaining cations are 7-fold-coordinated by the nearest anions, as shown in Figure 1d. The Brillouin zones (BZs) of the simulated crystal structures are drawn and shown in Figure S1.

3. COMPUTATIONAL DETAILS

The calculations were performed in the Quantum Espresso package,²³ wherein generalized gradient approximation (GGA) exchange–correlation functionals parameterized with the Perdew–Burke–Ernzerhof (PBE) method²⁴ were used along with the projector-augmented wave (PAW) pseudopotentials.²⁵ The following were taken as the valence electrons for the calculations: (1) Hf: $5s^2 6s^2 5p^6 5d^2$, (2) Zr: $4s^2 5s^2 4p^6 4d^2$, (3) O: $2s^2 2p^4$, and (4) N: $2s^2 2p^3$. The BZ sampling was performed based on the Monkhorst–Pack k and q -point grid.²⁶ The phonon frequencies were calculated based on the density functional perturbation theory (DFPT).²⁷ A very small self-consistency threshold (10^{-14} Ry) was used for the sensitive phonon calculations.

For both electronic and phononic calculations in $\gamma\text{-Hf}_2\text{ON}_2$ ($\gamma\text{-Zr}_2\text{ON}_2$), the energy cutoff (E_{cut}) and the charge density cutoff (ρ_{cut}) values were 90 Ry (80 Ry) and 1080 Ry (960 Ry), respectively. A large value of ρ_{cut} (12 times E_{cut}) was used to make sure that there is very little error in the phonon calculation. A $6 \times 6 \times 6$ k -point mesh was used for the electronic band calculations, while $2 \times 2 \times 2$ q -mesh (corresponding to 5 q points) was used for calculating normal phonon modes in the phonon band calculations.

For the $\beta\text{-M}_7\text{O}_8\text{N}_4$ system, an E_{cut} of 70 Ry, a ρ_{cut} of 840 Ry, and a k -point mesh of $3 \times 3 \times 3$ were used. The phonon calculation was performed at 14 q points in $\beta\text{-Hf}_7\text{O}_8\text{N}_4$ (corresponding to a $3 \times 3 \times 3$ q -point grid). The same was performed at 8 q points only (corresponding to the $2 \times 2 \times 2$ q -point grid) in $\beta\text{-Zr}_7\text{O}_8\text{N}_4$ to save the computing resources. This did not reduce the quality and reliability of the results, as will be seen later in Section 4.3. The E_{cut} and k -point values were finalized after a convergence test in each calculation. A description of the convergence test is provided in Figure S2, in which an E_{cut} of $\gamma\text{-Zr}_2\text{ON}_2$ is shown as an example.

There were eight formula units of $\gamma\text{-M}_2\text{ON}_2$ (40 atoms) in the simulated conventional unit cell. The metal atoms occupied 8a, 8c, 8d, and 8e, while the anions occupied 16f Wyckoff positions of $Ibca$. The starting atomic positions were adopted from Bredow and Lerch,²⁰ which were subsequently optimized for the final calculations. For $\beta\text{-M}_7\text{O}_8\text{N}_4$, three formula units (57 atoms) were simulated within the conventional unit cell. Starting atomic positions were taken from Bredow and Lerch²² for simulating in $P1$ (triclinic) setting. The coordinates and the path of the high-symmetry points in the BZ were taken from Setyawan and Curtarolo.³⁵

4. RESULTS AND DISCUSSION

4.1. Crystallographic and Electronic Properties. Some crystallographic and electronic data are listed in Table 1. The lattice constant values from our work match well with other theoretical and experimental works. The E_g value for $\gamma\text{-Hf}_2\text{ON}_2$ ($\gamma\text{-Zr}_2\text{ON}_2$) is 2.12 eV (1.66 eV). We also performed the calculations, allowing for the spin–orbit coupling (SOC) in both Zr and Hf compounds in the γ -phase. The results are presented in Note S1 and Table S1, which show that the fully relaxed lattice is undistorted when SOC is introduced as compared to the slightly distorted structures without the SOC.

Table 1. Crystallographic and Electronic Data of Hf and Zr Oxynitrides^a

	γ -Zr ₂ ON ₂	β -Zr ₇ O ₈ N ₄	γ -Hf ₂ ON ₂	β -Hf ₇ O ₈ N ₄
lattice	cubic bixbyite (modeled as <i>Ibca</i> [73])	rhombohedral, $R\bar{3}$ [148] (modeled as triclinic <i>P1</i>)	cubic bixbyite (modeled as <i>Ibca</i> [73])	rhombohedral, $R\bar{3}$ [148] (modeled as triclinic <i>P1</i>)
lattice parameter (Å)	<i>a</i>	10.136 ^{b,d} , 10.141 ^e , 10.125 ^f , 10.175 ^g , 10.220 ^h	9.625 ^d , 9.540 ^e , 9.540 ^f , 9.570 ^k , 9.538 ^k	9.972 ^{b,d} , 10.069 ^f , 9.880 ^h
	<i>b</i>	10.197 ^{b,d}	^c 9.574 ^d	10.033 ^{b,d}
	<i>c</i>	10.199 ^{b,d}	8.919 ^d , 8.846 ^e , 8.846 ^f , 8.880 ^{*k} , 8.850 ^{**k}	10.026 ^{b,d}
electronic band gap (eV)	1.66 ^d , 2.50 ^g , 1.50 ⁱ , 1.9 ^{*i} , 2.6 ^{**i}	2.87 ^d , 4.4 ^k	2.12 ^d , 1.91 ^h , 2.83 ^l	3.36 ^d , 3.66 ^l
direct band gap at Γ	1.77 ^d	2.90 ^d	2.24 ^d	3.40 ^d

^aThe first-row values on each parameter (with superscript *d*) are from the current study (DFT). ^bDFT calculation of the current work shows that the γ phases are marginally different for *a*, *b*, and *c*. Although the crystal is cubic bixbyite, it is in line with the choice of the orthorhombic *Ibca* space group. ^cCurrent work shows that the symmetry of β phases is slightly lower than for the hexagonal axes setting of the trigonal Bravais lattice, which is consistent with the choice of the *P1* (triclinic) system for the calculation. However, *b* is marginally smaller than *a*. Note that this crystal system is also regarded as “pseudo-cubic” in the literature, as mentioned in the main text. ^eReference 15 (experimental). ^fReferences 3, 17 (experimental). ^gReferences 4, 20 (DFT). ^hReference 30 (DFT). ⁱReference 7 (* refers to DFT, ** refers to experimental). ^jReference 16 (experimental). ^kReference 22 (* refers to DFT, ** refers to experimental). ^lReference 2 (experimental).

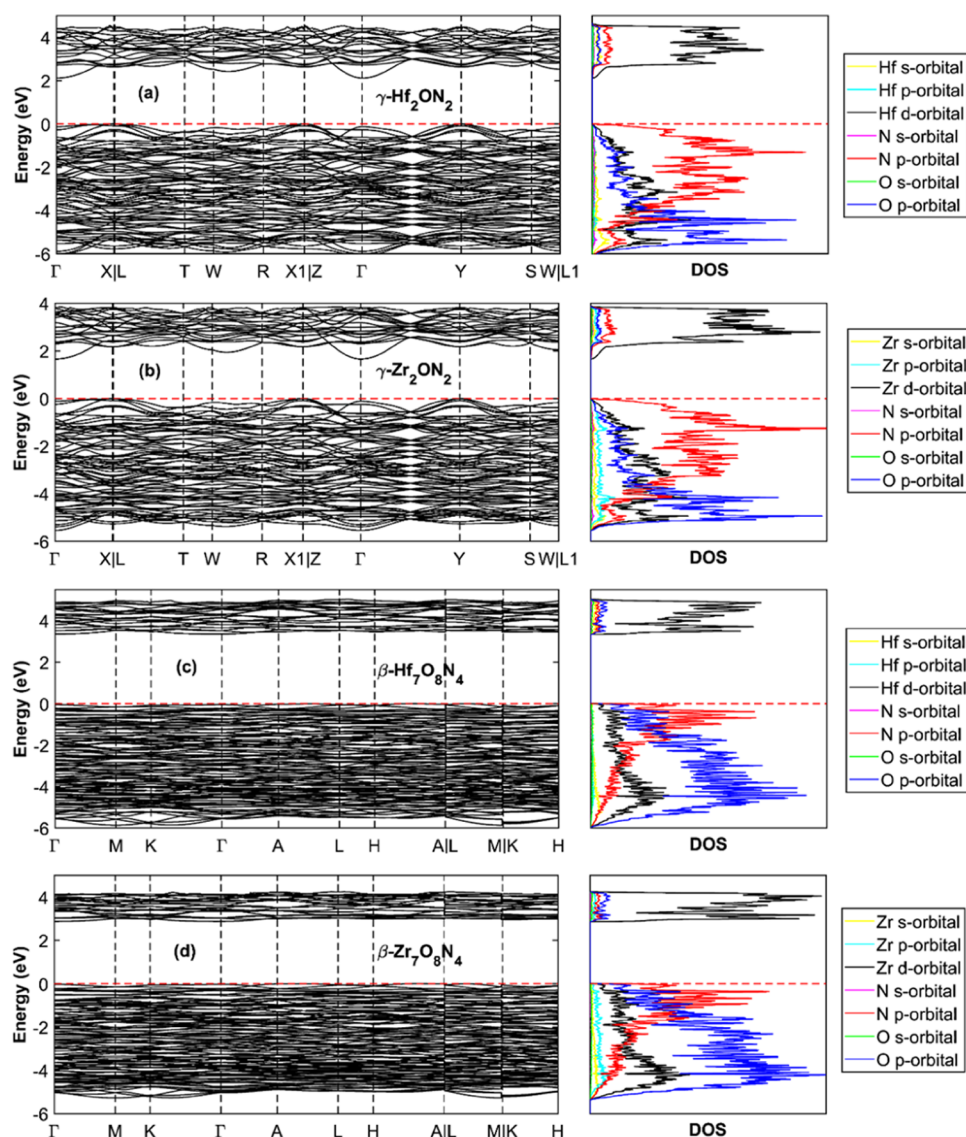


Figure 2. Electronic band dispersion. (a–d) γ -Hf₂ON₂, γ -Zr₂ON₂, β -Hf₇O₈N₄, and β -Zr₇O₈N₄, respectively. The right-hand side of each plot corresponds to the partial density of states.

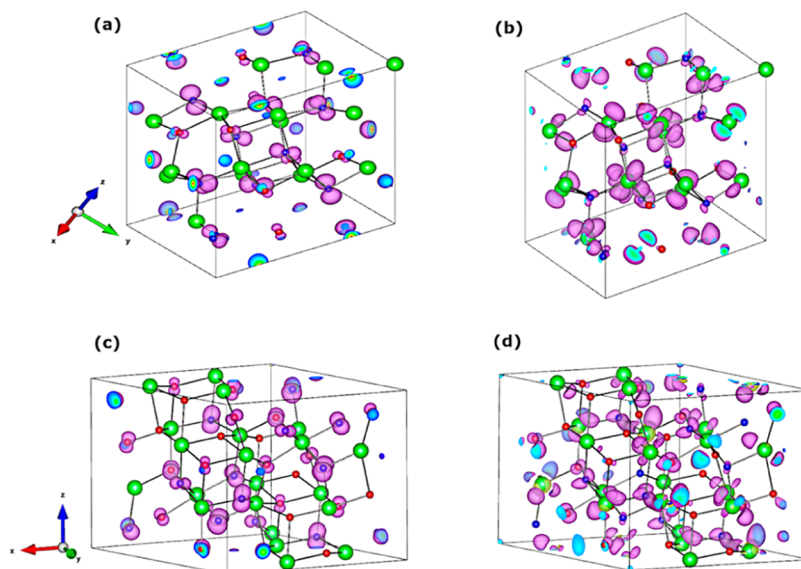


Figure 3. Isosurfaces of the Kohn–Sham orbitals. (a) At the valence band maximum of γ - Hf_2ON_2 . (b) At the conduction band minimum of γ - Hf_2ON_2 . (c) At the valence band maximum of β - $\text{Hf}_7\text{O}_8\text{N}_4$. (d) At the conduction band minimum of β - $\text{Hf}_7\text{O}_8\text{N}_4$.

The E_g value is also slightly reduced with SOC. We leave the further investigation of the SOC effect for future studies. The E_g values are underestimates compared to the experimental values, which is a common characteristic in a standard DFT method²⁸ but are in good agreement with the values reported in the referenced theoretical work. A closer to the experimental, but higher than the current band-gap values of γ - Zr_2ON_2 ²⁰ and β - $\text{Zr}_7\text{O}_8\text{N}_4$ ²² is attributed to the implementation of a hybrid DFT method in the referenced works. The same hybrid functionals predicted better intrinsic properties for some oxides than the other exchange–correlation methods such as PBE, the one that is employed here.²⁸ In Section 4.2, it will be seen that the calculated E_g values are matching with the optical characteristics; however, due to the implementation of the PBE functionals, the values may be underestimated. For much precise band-gap and optical values, hybrid functionals or Hubbard-corrected DFT (DFT + U)²⁹ methods can be tested. In this work, the focus is given to perform consolidated and simplified calculations and compare the properties among γ - and β -phases of the Hf and Zr counterparts; therefore, the choice of a certain type of exchange–correlation functional is noncritical.

The β -phases are more insulating than their corresponding γ -counterparts. This is intuitive because the oxynitride systems are related to the mixture of MO_2 and M_3N_4 in which the oxide phase has a higher E_g than the nitride phase and if the O (N) proportion is maintained, E_g of the oxynitride will increase (decrease). O in the β -phase is 42.11%, which is more than double the γ -phase (20%); hence, it has higher E_g . An interesting observation is that the indirect E_g values in the β -phases are \sim 1% away from the direct gap at the Γ point. Therefore, the band gap is a “pseudo-direct” type in the β -phase. On the other hand, the difference is greater than 5% in the γ -phase, so they are classed as having indirect E_g .

Figure 2 shows the calculated electronic band dispersion and partial electronic density of states (DOS) of both types of oxynitrides. The E_g is indirect in all oxynitrides. The partial DOS of the isostructural oxynitrides are similar to each other; however, there are differences between the β - and γ -phases. In γ - M_2ON_2 (Figure 2a,b), the top of the valence band (VB) is

primarily due to the N p-orbitals (red curves), while the O p-states (blue curves) occupy rather deeper levels and are strongly hybridized with the metal d-states. In β - $\text{M}_7\text{O}_8\text{N}_4$ (Figure 2c,d), the N p-orbital contribution shrinks as we move below the VB maximum, which is accompanied by a simultaneous increase in the O p-states. A strong hybridization of the N and O p-states near the VB maximum can be seen in the β -phases. Contribution from M d-states (black curves) is significant and similar from the top of the VB to deeper levels in all phases, while the conduction band (CB) minimum and higher states are mainly due to these M d-states. A distinguishing feature in the CB can be seen between the γ - and β -phases. In the γ -phase, a CB tail can be seen, which is completely absent in the β -phase, therefore widening the band gap. This may be related to the reduction in the Hf or Zr atomic proportion, from 40% in the γ -phase to 36.8% in the β -phase. We assume that the presence of more metallic cations in the γ -phase (as compared to the β -phase) lowers the band gap with the occurrence of the CB tail, which is similar to, for an example, that in $\text{Cu}_2\text{ZnSnS}_4$ (CZTS) solar cell where Sn-rich composition shows a band-gap shrinkage with a band tail.³¹

In all phases, N and O electronic contributions in the CBs are marginal but exhibit an interesting feature: in the γ -phases, the contribution due to the N p-states is almost double that of the O p-states (this is comparable to the atomic contribution of N, 40% and O, 20% in this phase), while there is no substantial difference in the β -phases although N (21.1%) is almost half of the O (42.1%). The effect of the s-orbitals on the electronic band diagram is not significant except in the very deep VB region where the majority of the dispersion is due to the N s-states (see Figure S3).

The observation that the N electronic states dominate over the O states near the VB maximum in all of these oxynitrides can be attributed to the larger number of partially filled 2p-states in N than in O. (There are three unpaired 2p-states in N and two unpaired 2p-states in O per atom.) However, in the β -phase, which has almost double the O-to-N atomic proportion as compared to the γ -phase, the higher O electronegativity should have an effect, which causes the O states to be closer to the core (nucleus) than the N states.

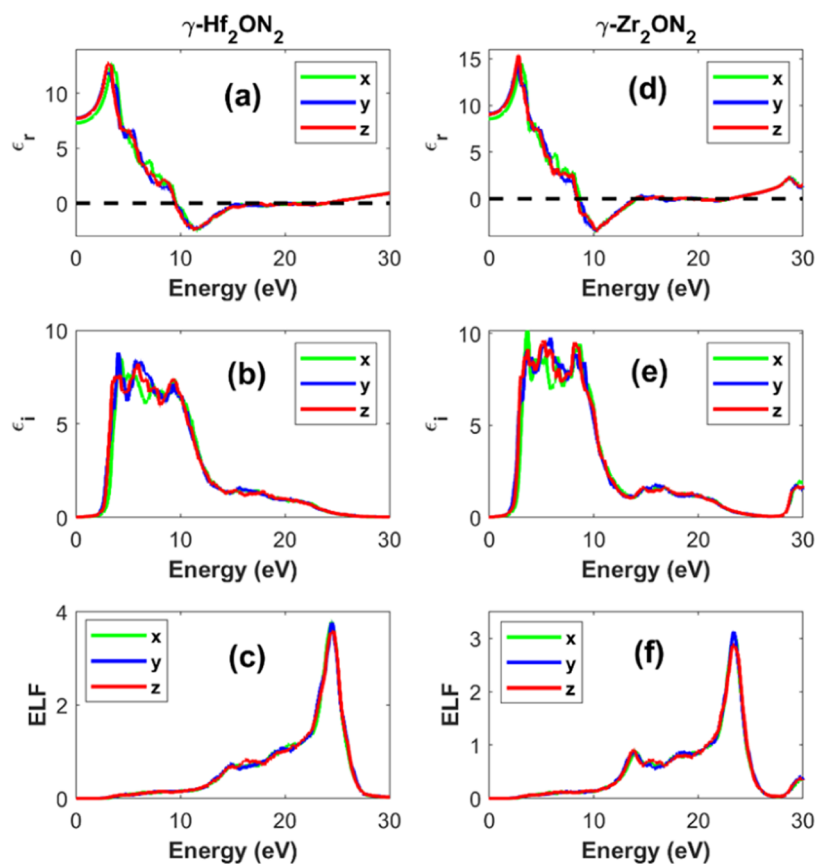


Figure 4. Optical properties. (a, d) Calculated real part of the dielectric function. (b, e) Calculated imaginary part of the dielectric function. (c, f) Calculated electron energy loss spectra. Panels (a–c) are for γ -Hf₂ON₂ and panels (d–f) are for γ -Zr₂ON₂. The properties are polarized in the *x*, *y*, and *z* axes corresponding to the parallel bixbyite crystallographic axes: *a*, *b*, and *c* directions.

The isosurfaces of Kohn–Sham orbitals at the VB maximum (equivalent to the HOMO in molecular systems) and the CB minimum (equivalent to LUMO in molecular systems) can be visualized in Figure 3, which combines the directional information extracted from the reciprocal space to the DOS in Figure 2. The diagrams are for the hafnium compounds, but their zirconium counterparts have the same characteristics and are presented in Figure S4. These density contour maps are consistent with the discussion in the previous paragraph and with the DOS of Figure 2. For the VB maximum (Figure 3a,c), the p-orbital electrons are concentrated around the N and O atoms (see the purple dipole-shaped isosurfaces around blue N and red O atoms). The size of the dipole is bigger around the N atoms, which is consistent with the higher partial DOS at the VB maximum in Figure 2. In the CB minimum (Figure 3b,d), metal d-states are dominant (see the purple quadrupoles around the green metal atoms). Small-sized N and O 2p-states are also visible in the CB minimum. The size of the N p-orbital is bigger than the O p-orbital in the γ -phase (Figure 3b), while they are similar in the β -phase (Figure 3d); this is consistent with the partial DOS in the CB, as shown in Figure 2. Another peculiar characteristic can be seen around the metal cation in the CB minimum (Figure 3b,d). The isosurfaces around the metal look more symmetric and ordered in the γ -phase as compared to those in the β -phase, where the charge density shapes seem distorted. We attribute this to having two dissimilar metal cations along the *c*-axis of the Bevan cluster for which one cation (at the center of the Bevan cluster) is

coordinated by six and the other is coordinated by seven anions, as described in Section 2 and Figure 1d.

4.2. Optical Properties. In this paper, optical properties are calculated for the γ -phases only. All other computational methods were similar except the choice of pseudopotentials in the optical property calculation where optimized norm-conserving Vanderbilt pseudopotentials have been used.³² The calculations were performed on 2744 equally weighted *k*-points generated by a $14 \times 14 \times 14$ Monkhorst–Pack *k*-grid in the first BZ.

The material's response to electromagnetic radiation is described by the frequency-dependent dielectric function $\epsilon(\omega) = \epsilon_r(\omega) + i\epsilon_i(\omega)$. (The bracketed omega (ω) will be avoided for simplicity from now on wherever possible.) This governs the propagation of light in a material, and many other micro-to-macroproperties such as refractive index (*n*), absorption coefficient (α), reflectivity (*R*), and transmittance depend on this. The imaginary part (ϵ_i) of the dielectric function characterizes the absorption of light and can be readily obtained from the electronic structure calculation, while the real part (ϵ_r) is obtained from the Kramers–Kronig transformation.³³ All other optical properties can then be obtained from simple relations based on the dielectric functions. The following set of equations show the relations for *n*, *k*, α , and *R*

$$n = \left[\frac{\epsilon_r}{2} + \sqrt{\frac{\epsilon_r^2 + \epsilon_i^2}{2}} \right]^{1/2} \quad (1)$$

$$k = \left[-\frac{\epsilon_r}{2} + \frac{\sqrt{\epsilon_r^2 + \epsilon_i^2}}{2} \right]^{1/2} \quad (2)$$

$$\alpha = \frac{4\pi k}{\lambda} \quad (3)$$

$$R = \frac{(1 - n)^2 + k^2}{(1 + n)^2 + k^2} \quad (4)$$

Although α and R are dependent on the fundamental optical values, they were calculated and presented in this study because these are the properties that are conveniently measured in labs and hence it will facilitate a direct comparison.

Figure 4 shows ϵ_r , ϵ_i , and the electron energy loss function (ELF) of γ -M₂ON₂. The energy edge of ϵ_i matches very well with the calculated E_g in both compounds. In the ϵ_r spectra, only one principal peak can be seen at ~ 3.3 eV (~ 2.8 eV) in γ -Hf₂ON₂ (γ -Zr₂ON₂), which is close to the corresponding E_g value. Therefore, these peaks can be assigned to the transition of valence electrons from mainly N 2p to metal d-states in the high-symmetry points of the first BZ. Because the γ -M₂ON₂ crystal deviates slightly from an ideal cubic system, the dielectric constant has different x , y , and z components, parallel to a , b , and c axes, respectively. The anisotropy related to this can be evaluated by calculating a ratio called the “static optical anisotropy” (A_{opt})^{34,36} using eq 5

$$A_{\text{opt}} = \left[\frac{\epsilon_{\text{rd}}(0)}{\epsilon_{\text{r}}^{\text{poly}}(0)}, \frac{n_{\text{d}}(0)}{n^{\text{poly}}(0)} \right] \quad (5)$$

where the subscript “d” refers to directions x , y , or z axes and the superscript “poly” refers to the “polycrystalline” static dielectric constant and refractive index, which can be calculated with the following equation

$$\epsilon_{\text{r}}^{\text{poly}} = \left(\frac{\epsilon_{\text{rx}}^2 + \epsilon_{\text{ry}}^2 + \epsilon_{\text{rz}}^2}{3} \right)^{1/2} \quad (6)$$

where the dielectric constant variable ϵ_r should be changed to n for the polycrystalline refractive index.

The optical anisotropy (A_{opt}), static dielectric constant – $\epsilon_r(0)$, and static refractive index – $n(0)$ values are presented in Table 2. A value of $A_{\text{opt}} = 1$ indicates a completely cubic system, which is isotropic. With increased anisotropy, this

Table 2. Static Dielectric Constant, Refractive Index, and Optical Anisotropy of the γ -Phase Oxynitrides

		γ -Zr ₂ ON ₂	γ -Hf ₂ ON ₂
static optical constants	$\epsilon_{\text{r}}^{\text{poly}}(0)$	8.90	7.59
	$\epsilon_{\text{rx}}(0)$	8.55	7.29
	$\epsilon_{\text{ry}}(0)$	9.10	7.74
	$\epsilon_{\text{rz}}(0)$	9.05	7.71
	$n^{\text{poly}}(0)$	2.98	2.75
	$n_x(0)$	2.92	2.70
	$n_y(0)$	3.02	2.78
	$n_z(0)$	3.00	2.78
	optical anisotropy	x	[0.961, 0.980]
y		[1.022, 1.011]	[1.021, 1.011]
z		[1.017, 1.008]	[1.017, 1.008]

value diverges away from 1. It is clear from Table 2 that the γ -phases are almost isotropic, which is indeed consistent with their being represented by the cubic bixbyite type, as mentioned in Section 2. The static optical values are higher for γ -Zr₂ON₂ than for γ -Hf₂ON₂, which is consistent with its inverse relationship with E_g .³⁴ These values are slightly smaller than the purely semiconducting nitrides (c-M₃N₄)³⁷ and are comparable to the family of superhard spinel nitrides³⁸—indicating why these oxynitrides have excellent hardness.

Figure 5 shows n , α , and R of these compounds. Refractive index quite naturally follows a similar trend to ϵ_r , as shown in Figure 4. From the maximum value of 3.63 (at 3.35 eV) and 3.97 (at 2.84 eV) for γ -Hf₂ON₂ and γ -Zr₂ON₂, respectively, in the c -direction, the refractive index falls sharply on either side of the energy spectra. (The trend is similar in the a and b directions with a marginal difference in the peak position.) This includes a continuous reduction in n in the visible to infrared spectra until it saturates for the static values in ~ 0 eV. The static refractive index value of γ -Hf₂ON₂ matches well with the experimentally measured value.² Again, the absorption edge in the α spectra is consistent with the respective E_g values and increases continuously until an absorption maximum is reached at an energy slightly higher than 10 eV for both materials. The locations of these maximum absorption peaks match with the maximum reflectivity, suggesting that around these energies, there will be very little photon transmission. There is an important relation between the ELF and the R spectra. The prominent peak in ELF, which defines the screened plasma frequency ω_p of the material, is accompanied by the trailing edge in the reflectivity curve.^{34,36} This is clearly observable in Figures 4 and 5 (the third-row subplots in each figure). In Figure S5, n , α , and R are reproduced and presented as a function of wavelength in a typical UV–vis–NIR region so that they are easily comparable with experimental data when required.

4.3. Phononic Properties. The phonon dispersions are presented in Figure 6. For full dispersion, please see Figure S6. The red curves in the dispersions are the three acoustic modes. In both γ - and β -phases, the slopes of the acoustic phonons are steeper in Zr than in Hf oxynitride. This is indicative of a slower speed of sound in the Hf oxynitrides as compared to their Zr counterparts. Apart from this, there are two observable significant results from the phonon dispersion: (1) there is a phonon band gap in γ -Hf₂ON₂ and (2) β -M₇O₈N₄ have imaginary phonon frequencies near the Γ point.

In Figure 6a, the phonon band gap appears to be between optical phonons only; however, the phonon DOS on the right-hand side shows that the phonon branches up to the top of the lower phonons below the gap (i.e., up to ~ 250 cm⁻¹) are due to the vibration of Hf atoms only. Because there were 8 formula units of γ -Hf₂ON₂ in the simulation, the lattice constant of the simulated unit cell is larger than that of the primitive unit cell, which imposed back-folding of the acoustic phonons and hence these are observed as “optical-like” phonons in the dispersion. Indeed, these optical-like acoustic phonons are presented in all four materials, which can be confirmed by the spreading of the metal partial phonon DOS (magenta curves) in all diagrams.

The negative phonon modes (also known as soft modes) obtained from a DFPT method are related to lattice instability either due to ferroelectric behavior or due to pressure- or temperature-dependent phase transitions.²⁷ No such study regarding the lattice instability of the β -M₇O₈N₄ has ever been

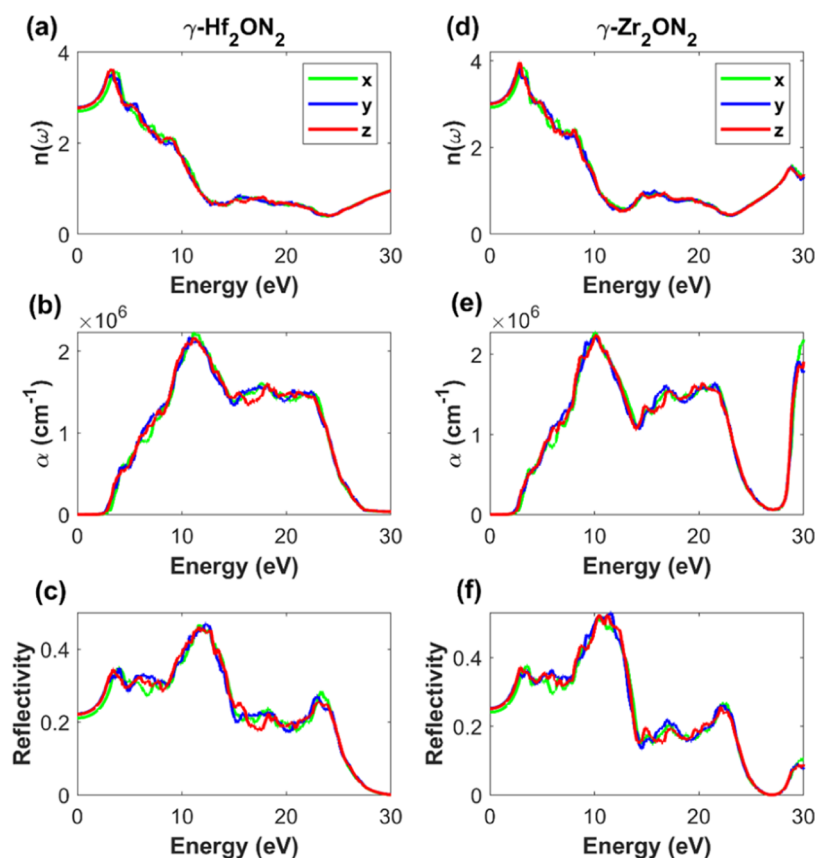


Figure 5. Optical properties. (a, d) Refractive index. (b, e) Absorption coefficient. (c, f) Reflectivity. Panels (a–c) are for γ -Hf₂ON₂ and panels (d–f) are for γ -Zr₂ON₂. The properties are polarized in the x , y , and z axes corresponding to the parallel bixbyite crystallographic axes: a , b , and c , respectively.

reported before. However, it can be speculated that the small soft mode near the zone center of the β -phases is likely to be due to a ferroelectric characteristic. Ferroelectricity, which is characterized by a robust switchable polarization, occurs when there is a constant interplay of the constituent species such as rotations and distortions from their ideal sites in the lattice. The ferroelectric phase of a material is characterized by a long-range Coulomb attraction, which occurs in a low-symmetry phase at lower temperature, while at higher temperature short-range repulsion becomes dominant and a high-symmetry phase is stabilized.^{39,40} For example, in BaTiO₃, a typical ferroelectric oxide perovskite, three ferroelectric phase transitions occur: from cubic to tetragonal at 393 K, tetragonal to orthorhombic at 278 K, and from orthorhombic to rhombohedral at 183 K.³⁹ At this point, two important points should be noted: (1) β -phases, which are rhombohedral, are basically formed by substituting some of the O vacancies by N anions in the cubic MO₂ structure and the structure (X-ray diffraction data) looks similar to each other (hence the term “pseudo-cubic”),^{2,22} and (2) as mentioned earlier, the building block of this structure (the Bevan cluster) has two types of metal cations, which create a constant struggle between the pseudo-cubic and rhombohedral metal sublattice to bring the symmetry to a perfect cubic or to further distort upon the application of some external force.^{21,41} Therefore, the β -phase is likely to rearrange to a highly symmetric cubic phase at a certain temperature, and because of the two dissimilar cations in the sublattice, there is likely to be relative movements that lead to the formation of electrical polarization as in oxide perovskites.⁴² While these are

as yet only speculations, this certainly invites detailed experimental characterization in the near future.

The presence of a phonon band gap in γ -Hf₂ON₂ and the qualitative indication of a smaller speed of sound also invites further studies in this material. These are preliminary indications of the material having a small thermal conductivity value, which is desirable in the HCSC and in thermoelectric materials. However, the small phonon band gap in γ -Hf₂ON₂ makes it unsuitable as a hot carrier absorber material because one of the most critical conditions for a hot carrier absorber is to have a suppressed Klemens decay mechanism,⁴³ an anharmonic scattering mechanism in which an optical phonon decays into two acoustic phonons of the same energy and equal and opposite momenta. Therefore, the minimum optical phonon frequency must be higher than twice the maximum acoustic phonon frequency to prevent the energy loss via Klemens decay—none of the studied oxynitrides meet this condition. Additionally, the higher E_g values in these oxynitrides make them unsuitable as a bulk hot carrier absorber material. Nevertheless, a recent publication shows that a high E_g material is a potential candidate for an energy-selective contact (ESC) of the HCSC concept.⁴⁴ Therefore, there are many areas where the electronic and phononic properties of these oxynitrides can be exploited, for example, the ESCs.

5. CONCLUSIONS

Hafnium and zirconium oxynitrides have potential applications in many areas such as semiconducting, optoelectronic, and PV

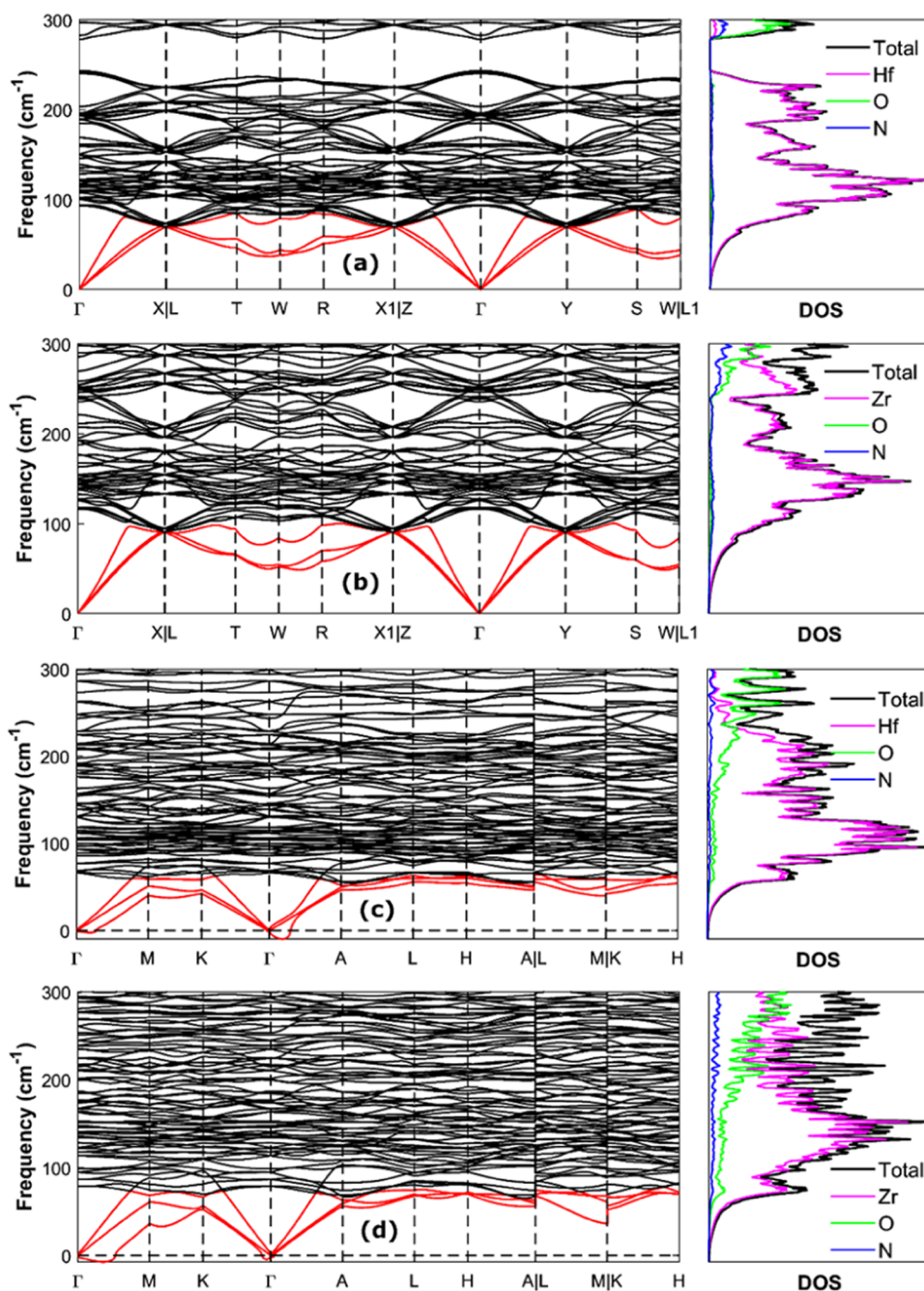


Figure 6. Phononic band dispersion. (a–d) γ - Hf_2ON_2 , γ - Zr_2ON_2 , β - $\text{Hf}_7\text{O}_8\text{N}_4$, and β - $\text{Zr}_7\text{O}_8\text{N}_4$, respectively. The right-hand side on each plot is the corresponding density of states.

devices. Here, we performed DFT calculations on electronic, optical, and phononic properties of the γ - and β -phases of Hf and Zr oxynitrides and present the consolidated results. The calculated lattice parameters, energy gap, and optical constant values match well with some available experimental and theoretical values. Our results show that the γ -phases have a purely indirect-type band gap and are characterized by a metallic d-state CB tail, while the β -phases have a pseudo-direct energy gap. We present various optical properties of the γ -phases and show that they are highly isotropic. The phononic properties of γ - Hf_2ON_2 exhibit a small gap in the phonon dispersion, and we observe soft phonon modes in β - $\text{M}_7\text{O}_8\text{N}_4$ indicating lattice instability. The emphasis is given if the phononic properties of these oxynitrides are favorable for the

use as a HCSC absorber material. Our results show that they cannot be used as a bulk HCSC absorber material; however, they look suitable for the ESCs of the HCSC and in many other applications.

■ ASSOCIATED CONTENT

Supporting Information

The Supporting Information is available free of charge at <https://pubs.acs.org/doi/10.1021/acsomega.1c05649>.

Cohesive energy and formation enthalpy for all phases; Brillouin zone shapes of the simulated structures; cutoff energy convergence test; partial electronic density of states in the whole spectra; Kohn–Sham orbitals for the Zr compounds; optical properties in the UV–vis–NIR

region; and full phonon dispersion for all simulated compounds (PDF)

AUTHOR INFORMATION

Corresponding Author

Bharat Thapa — School of Photovoltaic and Renewable Energy Engineering, UNSW, Sydney, NSW 2052, Australia;
orcid.org/0000-0002-0518-9506; Email: bhathapa@gmail.com, bharat.thapa@unsw.edu.au

Authors

Robert John Patterson — School of Photovoltaic and Renewable Energy Engineering, UNSW, Sydney, NSW 2052, Australia

Gavin Conibeer — School of Photovoltaic and Renewable Energy Engineering, UNSW, Sydney, NSW 2052, Australia

Santosh Shrestha — School of Photovoltaic and Renewable Energy Engineering, UNSW, Sydney, NSW 2052, Australia

Complete contact information is available at:

<https://pubs.acs.org/10.1021/acsomega.1c05649>

Author Contributions

B.T.: conceptualization, data curation, formal analysis, methodology, software, visualization, and writing (original draft); R.J.P.: resources, software, validation, and writing (review and editing); G.C.: resources, supervision, validation, and writing (review and editing); and S.S.: resources, supervision, validation, and writing (review and editing).

Notes

The authors declare no competing financial interest.

ACKNOWLEDGMENTS

This research was supported (partially or fully) by the Australian Government through the Australian Research Council. The views expressed herein are those of the authors and are not necessarily those of the Australian Government or Australian Research Council. The authors acknowledge UNSW IT support for computing time on the NCI Gadi computer cluster and UNSW Katana cluster.

REFERENCES

- (1) Kim, S. K.; Kim, Y.; No, K. Local structures and electronic structures of HfO₂N thin films: x-ray absorption fine structure study and first-principles calculations. *X-Ray Spectrom.* **2006**, *35*, 287–295.
- (2) Ino, T.; Kamimuta, Y.; Suzuki, M.; Koyama, M.; Nishiyama, A. Dielectric Constant Behavior of Hf–O–N System. *Jpn. J. Appl. Phys.* **2006**, *45*, 2908–2913.
- (3) Liu, W.; Su, X.-p.; Zhang, S.-y.; Wang, H.-b.; Liu, J.-h.; Yan, L.-q. Effect of the oxygen fraction on the structure and optical properties of HfO_xNy thin films. *Vacuum* **2008**, *82*, 1280–1284.
- (4) Rawal, S. K.; Chawla, A. K.; Jayaganthan, R.; Chandra, R. The influence of various sputtering parameters on structural, wettability and optical properties of Zr₂ON₂ thin films. *Mater. Sci. Eng. B* **2014**, *181*, 16–23.
- (5) (a) Jiang, S.; Liu, Y.; Xu, J. Rare earth oxynitrides: promising visible-light-driven photocatalysts for water splitting. *Mater. Adv.* **2021**, *2*, 1190–1203. (b) Black, A. P.; Suzuki, H.; Higashi, M.; Frontera, C.; Ritter, C.; De, C.; Sundaresan, A.; Abe, R.; Fuertes, A. New rare earth hafnium oxynitride perovskites with photocatalytic activity in water oxidation and reduction. *Chem. Commun.* **2018**, *54*, 1525–1528. (c) Fuertes, A. Nitride tuning of transition metal perovskites. *APL Mater.* **2020**, *8*, No. 020903.
- (6) Sakar, M.; Prakash, R. M.; Shinde, K.; Balakrishna, G. R. Revisiting the materials and mechanism of metal oxynitrides for photocatalysis. *Int. J. Hydrogen Energy* **2020**, *45*, 7691–7705.
- (7) Mishima, T.; Matsuda, M.; Miyake, M. Visible-light photocatalytic properties and electronic structure of Zr-based oxynitride, Zr₂ON₂, derived from nitridation of ZrO₂. *Appl. Catal., A* **2007**, *324*, 77–82.
- (8) Hisatomi, T.; Kubota, J.; Domen, K. Recent advances in semiconductors for photocatalytic and photoelectrochemical water splitting. *Chem. Soc. Rev.* **2014**, *43*, 7520–7535.
- (9) (a) Kang, C. S.; Cho, H.-J.; Onishi, K.; Nieh, R.; Choi, R.; Gopalan, S.; Krishnan, S.; Han, J. H.; Lee, J. C. Bonding states and electrical properties of ultrathin HfO_xNy gate dielectrics. *Appl. Phys. Lett.* **2002**, *81*, 2593–2595. (b) Puźniak, M.; Gajewski, W.; Zelechowski, M.; Jamroz, J.; Gertych, A.; Zdrojek, M.; Mroczynski, R. Technology and optimization of hafnium oxynitride (HfO_xNy) thin-films formed by pulsed-DC reactive magnetron sputtering for MIS devices. *Microelectron. Eng.* **2020**, *228*, No. 111332.
- (10) Yu, J.; Huang, W.; Lu, C.; Lin, G.; Li, C.; Chen, S.; Wang, J.; Xu, J.; Liu, C.; Lai, H. Resistive switching properties of polycrystalline HfO_xNy films by plasma-enhanced atomic layer deposition. *Jpn. J. Appl. Phys.* **2017**, *56*, No. 050304.
- (11) Valov, I.; Waser, R.; Jameson, J. R.; Kozicki, M. N. Electrochemical metallization memories—fundamentals, applications, prospects. *Nanotechnology* **2011**, *22*, No. 254003.
- (12) (a) Li, Y.; You, M.; Gong, X.; Li, X.; Lin, Z.; Liu, J. In *The Realization of ZrO_xNy Temperature Sensors With Good Sensitivity and Stability in the Temperature Range Above 150 K*, IEEE 16th International Conference on Nano/Micro Engineered and Molecular Systems (NEMS), 25–29 April, 2021; pp 1165–1168. (b) Lin, Z.; Li, X.; Zeng, Y.; You, M.; Wang, F.; Liu, J. The electronics transport mechanism of grain and grain boundary in semiconductive hafnium oxynitride thin film. *J. Mater. Sci.* **2020**, *55*, 2881–2890. (c) Lin, Z.; Zhan, G.; Li, X.; You, M.; Zeng, Y.; Wang, F.; Liu, J. The conduction process of grain and grain boundary in the semiconductive zirconium oxynitride thin film. *Semicond. Sci. Technol.* **2019**, *34*, No. 085008.
- (13) Thapa, B.; Dubajic, M.; Conibeer, G.; Shrestha, S. In *Synthesis and Characterisation of Hafnium Oxynitride Thin Film: Can It Be Used as a Hot Carrier Solar Cell Material?*, IEEE 48th Photovoltaic Specialists Conference (PVSC), 20–25 June, 2021; pp 1654–1658.
- (14) (a) Green, M. A. Third generation photovoltaics: Ultra-high conversion efficiency at low cost. *Prog. Photovoltaics* **2001**, *9*, 123–135. (b) Kahmann, S.; Loi, M. A. Hot carrier solar cells and the potential of perovskites for breaking the Shockley–Queisser limit. *J. Mater. Chem. C* **2019**, *7*, 2471–2486.
- (15) Lerch, M. Nitridation of Zirconia. *J. Am. Ceram. Soc.* **1996**, *79*, 2641–2644.
- (16) Lerch, M.; Krumeich, F.; Hock, R. Diffusion controlled formation of β type phases in the system ZrO₂–Zr₃N₄. *Solid State Ionics* **1997**, *95*, 87–93.
- (17) Clarke, S. J.; Michie, C. W.; Rosseinsky, M. J. Structure of Zr₂ON₂ by Neutron Powder Diffraction: The Absence of Nitride–Oxide Ordering. *J. Solid State Chem.* **1999**, *146*, 399–405.
- (18) Pialoux, A. Study of carbothermal reduction of hafnium dioxide by X-ray diffraction at high temperature. *J. Nucl. Mater.* **1993**, *200*, 1–10.
- (19) Nakhil, S.; Hermes, W.; Ressler, T.; Pöttgen, R.; Lerch, M. Synthesis, Crystal Structure and Magnetic Properties of Bixbyite-type Vanadium Oxide Nitrides. *Z. Naturforsch. B* **2009**, *64*, 281–286.
- (20) Bredow, T.; Lerch, M. Anion Distribution in Zr₂ON₂. *Z. Anorg. Allg. Chem.* **2004**, *630*, 2262–2266.
- (21) Locherer, T.; Dubrovinsky, L.; Fuess, H. Isothermal compression of nitrogen doped zirconia/zirconium oxynitride Zr₇O₁₁N₂ and equation of states. *Solid State Commun.* **2007**, *143*, 408–411.
- (22) Bredow, T.; Lerch, M. On the Anion Distribution in Zr₇O₈N₄. *Z. Anorg. Allg. Chem.* **2007**, *633*, 2598–2602.
- (23) Giannozzi, P.; Baroni, S.; Bonini, N.; Calandra, M.; Car, R.; Cavazzoni, C.; Ceresoli, D.; Chiarotti, G. L.; Cococcioni, M.; Dabo,

I.; et al. QUANTUM ESPRESSO: a modular and open-source software project for quantum simulations of materials. *J. Phys.: Condens. Matter* **2009**, *21*, No. 395502.

(24) Perdew, J. P.; Burke, K.; Ernzerhof, M. Generalized gradient approximation made simple. *Phys. Rev. Lett.* **1996**, *77*, No. 3865.

(25) (a) Blöchl, P. E. Projector augmented-wave method. *Phys. Rev. B* **1994**, *50*, 17953–17979. (b) Kresse, G.; Joubert, D. From ultrasoft pseudopotentials to the projector augmented-wave method. *Phys. Rev. B* **1999**, *59*, 1758–1775.

(26) Monkhorst, H. J.; Pack, J. D. Special points for Brillouin-zone integrations. *Phys. Rev. B* **1976**, *13*, 5188–5192.

(27) Baroni, S.; De Gironcoli, S.; Dal Corso, A.; Giannozzi, P. Phonons and related crystal properties from density-functional perturbation theory. *Rev. Mod. Phys.* **2001**, *73*, No. 515.

(28) Bredow, T.; Gerson, A. R. Effect of exchange and correlation on bulk properties of MgO, NiO, and CoO. *Phys. Rev. B* **2000**, *61*, 5194–5201.

(29) Floris, A.; Timrov, I.; Himmetoglu, B.; Marzari, N.; de Gironcoli, S.; Cococcioni, M. Hubbard-corrected density functional perturbation theory with ultrasoft pseudopotentials. *Phys. Rev. B* **2020**, *101*, No. 064305.

(30) Bazhanov, D.; Knizhnik, A.; Safonov, A.; Bagatur'Yants, A.; Stoker, M.; Korkin, A. Structure and electronic properties of zirconium and hafnium nitrides and oxynitrides. *J. Appl. Phys.* **2005**, *97*, No. 044108.

(31) Ma, S.; Li, H.; Hong, J.; Wang, H.; Lu, X.; Chen, Y.; Sun, L.; Yue, F.; Tamm, J. W.; Chu, J.; et al. Origin of Band-Tail and Deep-Donor States in Cu₂ZnSnS₄ Solar Cells and Their Suppression through Sn-Poor Composition. *J. Phys. Chem. Lett.* **2019**, *10*, 7929–7936.

(32) Hamann, D. R. Optimized norm-conserving Vanderbilt pseudopotentials. *Phys. Rev. B* **2013**, *88*, No. 085117.

(33) Chu, J.; Sher, A. *Physics and Properties of Narrow Gap Semiconductors*; Springer, 2008.

(34) Cherrad, D.; Maouche, D.; Boudissa, M.; Reffas, M.; Louail, L.; Maamache, M.; Haddadi, K.; Medkour, Y. Ultra soft pseudo potential investigation of fundamental physical properties of CaXO₃ (X = Sn and Hf) distorted perovskites: A reference study to the perfect perovskites. *Phys. B: Condens. Matter* **2013**, *429*, 95–105.

(35) Setyawan, W.; Curtarolo, S. High-throughput electronic band structure calculations: Challenges and tools. *Computational Materials Science* **2010**, *49* (2), 299–312.

(36) Liu, D.; Duan, Y.; Bao, W. Structural properties, electronic structures and optical properties of WB₂ with different structures: A theoretical investigation. *Ceram. Int.* **2018**, *44*, 11438–11447.

(37) Chihi, T.; Fatmi, M.; Ghebouli, B.; Guemaz, M. Theoretical prediction of the structural, elastic, electronic and optical properties of Zr₃N₄ and Hf₃N₄ compounds. *Solid State Sci.* **2011**, *13*, 1414–1419.

(38) Xu, M.; Wang, S.; Yin, G.; Li, J.; Zheng, Y.; Chen, L.; Jia, Y. Optical properties of cubic Ti₃N₄, Zr₃N₄, and Hf₃N₄. *Appl. Phys. Lett.* **2006**, *89*, No. 151908.

(39) Cohen, R. E. Origin of ferroelectricity in perovskite oxides. *Nature* **1992**, *358*, 136–138.

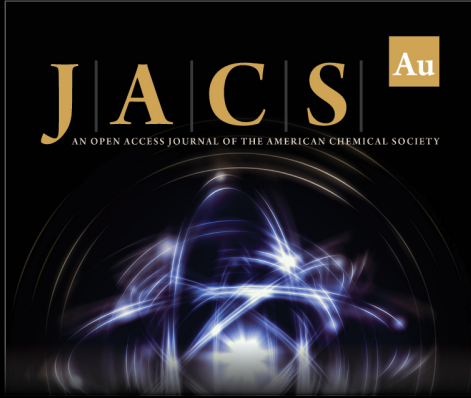
(40) Martin, L. W.; Rappe, A. M. Thin-film ferroelectric materials and their applications. *Nat. Rev. Mater.* **2017**, *2*, No. 16087.

(41) Locherer, T.; Dubrovinsky, L.; Fuess, H. Isothermal compressibility and thermal expansion of nitrogen doped hafnia Hf₇O₁₁N₂. *Solid State Commun.* **2009**, *149*, 2160–2163.

(42) Saha, S.; Sinha, T. P.; Mookerjee, A. Structural and optical properties of paraelectric SrTiO₃. *J. Phys.: Condens. Matter* **2000**, *12*, 3325–3336.


(43) Klemens, P. Anharmonic decay of optical phonons. *Phys. Rev.* **1966**, *148*, No. 845.


(44) Takeda, Y. Hot-carrier solar cells and improved types using wide-bandgap energy-selective contacts. *Prog. Photovoltaics* **2021**, *30*, 65.



JACS Au
AN OPEN ACCESS JOURNAL OF THE AMERICAN CHEMICAL SOCIETY

Editor-in-Chief
Prof. Christopher W. Jones
Georgia Institute of Technology, USA

Open for Submissions 

pubs.acs.org/jacsau  ACS Publications
Most Trusted. Most Cited. Most Read.